Supporting Information for "Laboratory Landquakes: Insights from experiments into the high-frequency seismic signal generated by geophysical granular flows"

M. I. Arran[1,*], A. Mangeney[1], J. De Rosny[2], M. Farin[2], R. Toussaint[3,4], O. Roche[5]

[1]Université de Paris, Institut de physique du globe de Paris, CNRS, F-75005 Paris, France

[2]Institut Langevin, ESPCI Paris, PSL University, CNRS, 75005 Paris, France

[3]Université de Strasbourg, CNRS, Institut Terre et Environnement de Strasbourg, UMR 7063, F-67084 Strasbourg, France

[4]SFF PoreLab, The Njord Centre, Department of Physics, University of Oslo, Oslo, Norway

[5]Université Clermont Auvergne, CNRS, IRD, OPGC, Laboratoire Magmas et Volcans, F-63000 Clermont-Ferrand, France.

[*]Corresponding author: Matthew Arran, arran@ipgp.fr

Contents of this file

1. Text S1 to S10
2. Figures S1 to S6
3. Table S1

Additional Supporting Information (Files uploaded separately)

1. Captions for Movies S1 to S2

0148-0227/21/$9.00

Introduction

To supplement the text of "Laboratory Landquakes", we gather here a collection of appendices to the text; figures and a table associated with these appendices; and descriptions of two videos that provide supplementary illustration. In section S1, we list and define the notation used in the article's text. Section S2 describes and justifies conditions for the validity of the 'stochastic impact' framework that's described in section 1.2, for predicting a granular flow's seismic signal, while section S3 reviews the use of Hertz theory to describe binary, elastic, quasistatic, normal interactions between spheres. We describe in sections S4 and S5, respectively, the amplifier settings used in experiments and the experimental control system, while sections S6 and S7 describe the derivation, calibration, and validation of relations linking experimental measurements to i) the net force applied by each flow to the instrumented plate and ii) the power spectrum of this force's normal component. Section S8 describes the processing of high-speed camera images to extract base-normal profiles of flow properties at the channel wall, S9 describes the statistical tools used to analyse our experimental results, and section S10 demonstrates the importance of the Green's function in the interpretation of landquake signals.

Figure S1 is associated with section S3, Figure S2 with section S5, Figure S3 with section S6, and Figures S4 and S5 with section S7. Table S1 is associated with section S9 and Figure S6 with section S10. Finally, the mp4 videos available as supplementary material illustrate section S8 and are described at Movie S1 and Movie S2.

S1. Notation

$f, t, \mathbf{x}$: Frequency, time, source position

$P_\cdot$: The power spectral density of a quantity $\cdot$

$\tilde{\cdot}$: The Fourier transform of $\cdot$ over time interval Δt

$\langle\cdot\rangle_{\Delta t}$: The arithmetic mean of $\cdot$ over the interval Δt

$\langle\tilde{\cdot}\rangle_{\Delta f}$: The moving average of $\tilde{\cdot}$ over a frequency window Δf

$v_{\mathbf{r}}$: The landquake velocity signal at a receiver at $\mathbf{r}$, radius r from the source

n_I: The number of impacts per unit volume and per unit time

$\mathbf{F}_I$: The force exerted by a representative impact

$\mathbf{G}$: The Green's function linking $\mathbf{F}_I$ to $v_{\mathbf{r}}$

A, ϕ: The area and particle volume fraction of a granular flow

ρ, d, u: The density, diameter, and downslope speed of a representative particle

$\Delta p, \mathbf{e}_I$: The magnitude and direction of the impulse of a representative impact

$h, \bar{u}$: The depth and depth-averaged mean velocity of a flow

E, ν: The Young's modulus and Poisson's ratio of a particle's material

$\tau(u_n)$: The timescale of a Hertzian impact at normal velocity u_n

ζ: The normalised, non-dimensional spectral density of the normal force betwen particles undergoing a Hertzian impact

u_j, T_j, z_j: The mean velocity, granular temperature, and base-normal position of particles in a flow's jth layer

h_g: The experimental flow's depth at its point of outflow from the reservoir

W, θ: The width and inclination angle of the experimental channel

X, Y, H: The length, width, and thickness of the instrumented plate

F_x, F_z: The downslope and base-normal forces exerted by the flow on the plate

g: The magnitude of gravitational acceleration

$t_d, \Delta t_c$: The time delay before, and the duration of, the high-speed camera's recording

σ: The average mass per unit area overlying the instrumented plate, over time Δt_c

μ: The effective friction between the instrumented plate and the overlying flow

M: The cumulative mass outflow through the channel, as measured by the mass balance

q: The average mass flux through the channel, per unit width, over time Δt_c

ρ_p, E_p, ν_p: The density, Young's modulus, and Poisson's ratio of the instrumented plate

D, Δ_f: The plate's bending stiffness and the mean frequency gap between its resonances

$\mathcal{P}$: The proportion of the plate's energy in its measurable vertical motion

Q: The quality factor for the attenuation of the plate's energy

a_j: The acceleration measured by the instrumented plate's jth accelerometer

$x_j, z_j, \mathbf{u}_j$: The downslope position, base-normal height, and velocity of a particle tracked at the channel's sidewall

$C(\cdot; z)$: A normalised coarse-graining function, localised around z

$\phi_w(z), \mathbf{u}_w(z), T_w(z)$: Depth-profiles of the mean relative volume fraction, velocity, and granular temperature of particles tracked at the channel's sidewall

$u_w, \bar{u}_w$: The downslope component of $\mathbf{u}_w$ and its depth-averaged value

P_F: The power spectral density of the normal force exerted by a flow on its base

P_F^0: The amplitude of P_F at signal periods much larger than the timescale of individual impacts but less than that of the flow's evolution

f_c: The corner frequency of P_F, at which it falls below half its maximum value

$\hat{\cdot}$: A model's prediction for the quantity $\cdot$

K: An unspecified prefactor in the model of Kean et al. (2015)

e: The coefficient of restitution of particles' impacts in the model of Farin, Tsai, Lamb, and Allstadt (2019)

υ: The normalised standard deviation of base-impacting particles' velocities

$\xi(\upsilon)$: A non-dimensional prefactor accounting for variation in impacts' geometry in the models of Farin et al. (2019)

χ: A shape factor for basal particle's mean downslope velocity, in the 'thick-flow' model

γ: A constant of attenuation, with an impact's base-normal height, for the squared impulse it transfers to the base, in the model of Bachelet et al.

ϵ: The typical factor of error in a model's predictions of P_F^0

$I, \hat{I}$: The inertial number within a flow and a bulk estimate for its value

δF: The high-frequency fluctuating force exerted by the flow on the instrumented plate

$\delta\mathcal{F}^2$: The ratio between i) the mean of δF^2 and ii) the squared mean force

Π_s: The total high-frequency seismic power transferred by the flow to the plate

ρ_g, c_s: The density and shear wave velocity of an idealised Earth

$t_r - t_s$: The source-receiver delay of an idealised Green's function

S2. The Stochastic Impact Framework

Here, we discuss the 'stochastic impact' framework: consideration of the total seismic signal as a sum of the uncorrelated signals generated by individual particle impacts, with the properties of the impacts determined by mean properties of the flow and with a specified Green's function mapping the force of an individual impact to the seismic signal observed at a remote station. By doing so, we hope to indicate its range of validity, by making clear the assumptions on which it rests: that the signal originates mainly from particle impacts; that materials are sufficiently stiff for the total signal to be the sum of signals from individual impacts; that the area considered is sufficiently extensive or the frequencies considered sufficiently high for impacts' signals to be uncorrelated; and that the spatial and temporal intervals between impacts are much smaller than the length and time scales of variation both of the flow and of the Green's function for signal propagation, so that a single impact force and Green's function may be used to represent all impacts.

S2.1. Impacts Must be the Dominant Source of the Signal

Most obviously, for a model of individual impacts to describe the seismic signal generated by a geophysical granular flow, other sources (e.g. those described by Michlmayr and Or (2014)) must be less significant. For example, we would not expect the model to apply to rockslides, for which basal friction is expected to be the dominant source, or to soil creep, for which the rupture of soil fibres would be more significant.

S2.2. The Signal Must be a Sum of Individual Impact Signals

Next, we must be able to consider impacts separately, with negligible interactions between them and hence a total signal equal to the sum of the individual signals. This will be the case if the deformation due to one impact at the site of a second is small compared to the local deformation due to that second impact. Or, writing $\epsilon(\mathbf{x}, \mathbf{x}_1)$ for deformation at x due to the impact at $\mathbf{x}_1$, we require $\epsilon(\mathbf{x}_2, \mathbf{x}_1) \ll \epsilon(\mathbf{x}_2, \mathbf{x}_2)$. Since $||\mathbf{x}_2 - \mathbf{x}_1||$ is at least a particle radius, this will be the case if deformation is limited to within a particle radius, so if the impacted material is sufficiently stiff. It will not be the case for, for example, rockfalls onto sandbeds, for which the crater caused by one rock's impact will affect the impact of another.

S2.3. Impact Signals Must be Uncorrelated

For the framework to work, we next require that the signals from different impacts must be uncorrelated in Fourier space. If, in frequency space, $\tilde{\mathbf{F}}_j$ is the force applied by an impact and $\tilde{\mathbf{G}}_j$ is the seismic station's response function, we require that, over $j \neq k$,

$$\mathbb{E}\left[\left(\tilde{\mathbf{F}}_j \cdot \tilde{\mathbf{G}}_j\right)\left(\tilde{\mathbf{F}}_k \cdot \tilde{\mathbf{G}}_k\right)\right] = 0, \tag{1}$$

where we write $\mathbb{E}$ for the expectation of a random variable. We describe two scenarios in which this will not be true and two methods for ensuring that it is.

First, we note that signals will, in general, be correlated at the low frequencies that correspond to the timescales of variation of the bulk flow. For example, if T is a time interval over which a flow runs into a southern valley wall and turns north, impacts during the turn will apply forces on the bedrock that, averaged over T, are directed southwards more often than northwards. At frequencies less than $1/2T$, the Fourier transforms of these forces will therefore tend to have the same sense, and so these impacts will - barring large phase differences in a seismic station's response - generate correlated signals. Similarly, signals will be correlated if impacts occur at regular intervals; a particle undergoing similar impacts at constant time intervals Δt_i will generate, at a seismic station with similar response functions to such impacts, correlated signals from the impacts at all frequencies that are multiples of $1/\Delta t_i$.

In both cases, the correlation can often be avoided by considering the total signal generated by a sufficiently large spatial and temporal extent. If the time over which the frequency-space signal is measured is longer than the time over which impacts are correlated (so that e.g. northwards-directed forces contribute to the total signal as much as southwards-directed ones) and the region considered extends beyond the lengths over which impacts are correlated (so that e.g. the total signal has contributions from other particles with the same Δt_i interval between impacts, but different phases), then correlations between close impacts will be cancelled out by anticorrelations between distant impacts, and the total correlation will be close to zero. However, consideration of larger spatial and temporal extents decreases resolution and makes the mean properties of the flow less representative of the local flow properties that determine individual impacts.

These problems can be avoided by considering the signals at higher frequencies. Informally, high-frequency signals can only be correlated if patterns in impact properties, such as the above examples, hold to an improbably high degree of precision in time. Formally, we can write the Fourier-space signal for the jth impact as $\tilde{v}_j(\omega)e^{-i\omega t_j}$ for angular frequency ω, with t_j the time at which the impact starts and with differences in $\tilde{v}_j$ linked only to differences in the physics governing each impact signal. If, for two impacts, the joint probability distribution of $\tilde{v}_j$, $\tilde{v}_k$ and $t_j - t_k$ is $f_P(\mathbf{v}, t)$, then the expected correlation between two different signals will be

$$\mathbb{E}\left[\tilde{v}_j^*(\omega)\tilde{v}_k(\omega)e^{i\omega(t_j - t_k)}\right] = \int_{\mathbb{C}^2 \times \mathbb{R}} v_1^* v_2 e^{i\omega t} f_P(\mathbf{v}, t) \mathrm{d}v_1 \mathrm{d}v_2 \mathrm{d}t. \tag{2}$$

Now, we write T for the time over which mean flow properties vary and $\sigma_{\Delta t}$ for the standard deviation of the interval between consecutive correlated impacts. For $\omega \gg 1/\sigma_{\Delta t}$ and $\omega \gg 1/T$, impacts will occur at a constant rate between t and $t + 1/\omega$ and the same physics is expected to apply to each impact, so $f_P(\mathbf{v}, t)$ will vary little over the timescale $1/\omega$. However, $e^{i\omega t}$ will have a mean value of zero over the same timescale, and consequently the integral in (2) will vanish, in the spirit of the Riemann-Lebesgue lemma. Therefore, we expect signals at periods much less than the timescales of flow variation or impact-time co-ordination to be uncorrelated. Such signals will be non-negligible if the duration of impacts is much less than these timescales and this will be the case if the materials involved in an impact are sufficiently stiff.

S2.4. Mean Properties Must Determine Impact Signals

Finally, for some mean properties of the flow to be linked via individual impacts' properties to the seismic signal observed at a remote station, we require the flow to be divisible into spatial and temporal domains that satisfy two properties. The domains must be a) large enough for the law of large numbers to apply to the signals from individual impacts within them, which can therefore be predicted using mean properties of each flow domain, but b) small enough that there is little variation in the magnitude of the remote station's response function to those signals, so that the same Green's function can be used for all such signals. Such domains will exist if the spatial and temporal intervals between impacts are much smaller than the length and time scales of variation of the flow or the Green's functions for signal propagation.

S3. Hertz Theory

We consider binary, elastic, quasistatic, normal interactions between spheres, which is the axisymmetric case of the problem introduced and solved by Hertz (1881). This is a strong set of assumptions, but we expect the derived results to be reasonable approximations, since the energetic collisions between glass beads which contributed most to the seismic signal exhibit a) short collision durations, so that a binary approximation is not unreasonable; b) restitution coefficients close to one, so that collisions are approximately elastic; c) impact speeds much less than the materials' speeds of sound, so that materials' internal deformation adjusts rapidly to changes of particle positions; and d) low friction coefficients, so that the normal forces between particles are much larger than the tangential forces. For homogeneous spheres with radii r_1 and r_2, Young's moduli E_1 and E_2, and Poisson's ratios ν_1 and ν_2, with centres separated by $r_1 + r_2 - \delta$, Hertz (1881) derives that the normal force between the particles is

$$F_n = \kappa \delta^{3/2}, \tag{3}$$

for κ related to harmonic means of the particles' properties by

$$\kappa = \frac{4}{3}\left(\frac{1-\nu_1^2}{E_1} + \frac{1-\nu_2^2}{E_2}\right)^{-1} \sqrt{\left(\frac{1}{r_1} + \frac{1}{r_2}\right)^{-1}}. \tag{4}$$

If the first particle has density ρ, the second particle is fixed, and the initial normal impact velocity is u_n, then δ satisfies for $m = 4\pi\rho r_1^3/3$ the Newtonian system of equations

$$\begin{aligned} \delta(0) &= 0, \\ \dot{\delta}(0) &= u_n, \\ m\ddot{\delta}(t) &= -\kappa\delta(t)^{3/2}. \end{aligned} \tag{5}$$

Noting that we have three parameters κ, m, and u_n in the three dimensions mass, length, and time, we can by the Buckingham π theorem (Bertrand, 1878; Buckingham, 1914) define typical length and time scales for the impact

$$\begin{aligned} \lambda &= \left(\frac{m u_n^2}{\kappa}\right)^{2/5} \\ &= \left[\pi^2\rho^2 u_n^4 \left(\frac{1-\nu_1^2}{E_1} + \frac{1-\nu_2^2}{E_2}\right)^2 \left(1 + \frac{r_1}{r_2}\right)\right]^{1/5} r_1, \end{aligned} \tag{6}$$

$$\begin{aligned} \tau &= \left(\frac{m^2}{\kappa^2 u_n}\right)^{1/5} \\ &= \left[\frac{\pi^2\rho^2}{u_n} \left(\frac{1-\nu_1^2}{E_1} + \frac{1-\nu_2^2}{E_2}\right)^2 \left(1 + \frac{r_1}{r_2}\right)\right]^{1/5} r_1, \end{aligned} \tag{7}$$

and can switch to a non-dimensional system of equations for $\Delta = \delta/\lambda$ as a function of $T = t/\tau$:

$$\begin{aligned} \Delta(0) &= 0, \\ \Delta'(0) &= 1, \\ \Delta''(T) &= -\Delta(T)^{3/2}. \end{aligned} \tag{8}$$

We solve these equations numerically, with Figure S1a indicating the evolution over time of the non-dimensional normal deformation Δ and force $\mathcal{F}_n = F_n/\kappa\lambda^{3/2}$, and Figure S1b showing the power spectrum $|\tilde{\mathcal{F}}_n|^2$ of that non-dimensional normal force.

We note that since the impact is elastic and of finite duration, the first particle's non-dimensional post-impact velocity is $\lim_{T\to\infty} \Delta'(T) = -1$, and so the zero-frequency limit of the basal force's Fourier spectrum is

$$\begin{aligned} \tilde{\mathcal{F}}_n(0) &= \int_{-\infty}^{\infty} -\Delta''(T)\, \mathrm{d}T \\ &= 2. \end{aligned} \tag{9}$$

We therefore define a non-dimensional function $\zeta(f\tau) = |\tilde{\mathcal{F}}_n(f\tau)|^2/4$, and note from the numerical solution (or else by the integrability, non-negativity, and symmetry of $\mathcal{F}_n$) that ζ is approximately equal to 1 for $f\tau \ll 1$, monotonically decreases to $\zeta(f_c\tau) = 0.5$ for a non-dimensional corner frequency that we calculate to be approximately $f_c\tau = 0.208$, and is much less than 1 for $f\tau > 1$.

Re-dimensionalising, we note that the spectral density of the normal force has units $\mathrm{kg}^2\,\mathrm{m}^2\,\mathrm{s}^{-2}$ and so that

$$|\tilde{F}_n(f)|^2 = (m u_n)^2 |\tilde{\mathcal{F}}_n(f\tau)|^2 = \left(\frac{\pi\rho d^3 u_n}{3}\right)^2 \zeta(f\tau), \tag{10}$$

while for beads with equal diameters d, Young's moduli E, and Poisson's ratios ν,

$$\tau = \left[\frac{\pi^2\rho^2(1-\nu_2^2)^2}{4E^2 u_n}\right]^{1/5} d. \tag{11}$$

For disparate particles, as in section S7.3, we can re-dimensionalise using mass m and the length and time scales defined in equations (6) and (7).

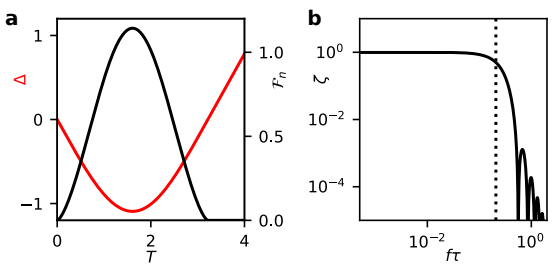

Figure S1. *Non-dimensional evolution of a Hertzian impact.* a) Evolution of the normal deformation Δ (red) and normal force $\mathcal{F}_n$ (black). b) Shape function ζ for the power spectral density $|\tilde{\mathcal{F}}_n|^2 = 4\zeta$ of normal force, with the corner frequency $f_c\tau$ indicated (dotted line).

S4. Amplifier Settings

Before the first experiment, we uploaded settings for the Kistler 5073 charge amplifier via an RS232 interface with the laboratory laptop, using the Python program `kistler_control.py` in the GitLab repository for this paper (Arran et al., 2021). With this program, we set the amplifier sensitivity to its maximal value of $0.1\,\mathrm{V\,pC}^{-1}$ and the amplifier bandwidth filter was turned off.

For each channel inclination and reservoir gate height, we set the settings of the Brüel and Kjær Nexus 2692-A-OS4 conditioning amplifier using its manual user interface. The nominal sensitivity of the accelerometers was set to $s_a = 0.006\,\mathrm{pC}\,/\,(\mathrm{m\,s^{-2}})$ and the nominal sensitivity of the amplifier to the highest value s_A among 3.16, 10, and $31.6\,\mathrm{mV}\,/\,(\mathrm{m\,s^{-2}})$ for which the amplifier's output remained below 10 V. We define $A = s_A/s_a$ for the true amplification. We set the corner frequencies of the amplifier's bandpass filter to their minimal and maximal values, respectively, of 10 Hz and 100 kHz.

S5. Experiment Control

We used a variety of programs to control the experiment and record data. At each channel inclination and release gate height, the program `run_experiment.ino` was uploaded to the microcontroller, with a defined experiment duration T_e, camera delay T_d, and camera footage duration T_c. Then, before each experiment, three programs started running in order to record data: Optronis' TimeViewer software to record camera footage at frame rate 2 kHz, subject to an external trigger and over duration T_c; the program `record_picoscope.exe` to record data from the oscilloscope at sample rate 250 kHz, with an external trigger and duration T_e set by settings file `exp_settings.txt`; and the program `record_balance.py` to record data from the mass balance at 5 Hz and over duration T_e, starting after a three-second beeped countdown and a 'go' beep. All programs are available on a GitLab repository associated with this paper (Arran et al., 2021).

Signals sent between the apparatus synchronised measurements. The `record_balance.py` program emitted a 'go' beep to mark the start of the experiment, upon which the experimentalist manually lifted the reservoir's release gate and pressed a start switch. This switch completed a circuit, increasing the voltage at the Arduino microcontroller's analogue input pin. The microcontroller responded by sending a digital signal to the force sensor amplifier and to the oscilloscope, and by starting a delay timer of duration T_d. In turn, the force sensor amplifier responded to the signal by switching to 'Measure' mode, amplifying the plate-normal, downslope, and cross-slope signals from the force sensor and transmitting them to the oscilloscope, for which the microcontroller's signal was the external trigger to start recording the signals from both the force sensor amplifier and the accelerometer amplifier, sending them to the Lenovo laptop. While the oscilloscope was recording data, the microcontroller reached the end of its time delay T_d and sent a digital signal to switch a relay, which in turn sent a trigger signal to the high-speed camera to initiate its recording, with data again sent to the laptop. Figure S2 is a schematic of this control system.

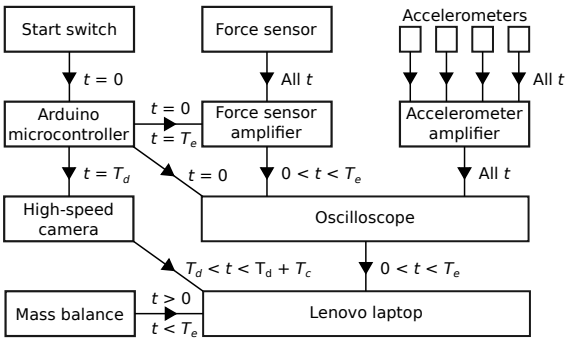

Figure S2. *Schematic of experimental control and measurement system.* The experiment is controlled and measurements recorded via signals sent between the labelled devices. Arrows indicate the signals sent between devices, with labels indicating the times at which they are sent.

S6. Calculation of the Net Force on the Instrumented Plate

Here, we describe our derivation, calibration, and validation of a relation between a) the net force applied by the flow to the instrumented plate, and b) the voltage outputs of the force sensor's charge amplifier.

S6.1. Derivation

The three voltage outputs from the force sensor's charge amplifier, after being downsampled to 200 Hz by averaging over 5 ms intervals, were each the sum of three components: a zero offset following the switch to the 'Measure' mode; an approximately linear drift over time due to charge build-up; and a signal from the sensor that was linear in the forces applied to the plate by the flow, but with cross-talk between the different components of force and with unknown coefficients. Writing the downsampled voltage and force as $\mathbf{V}(t)$ and $\mathbf{F}(t)$, there existed varying offset and drift vectors $\mathbf{V}^0$ and α, and a constant response matrix β, such that

$$\mathbf{V}(t) \approx \mathbf{V}^0 + \alpha t + \beta \mathbf{F}(t). \tag{12}$$

To recover the downslope and plate-normal forces applied to the plate, under the assumption that the contribution of the cross-slope force was negligible, we considered the two corresponding voltage outputs; directly removed the effect of the zero offset $\mathbf{V}^0$; subtracted the expected linear drift $\mathbb{E}\left[\hat{\alpha}\right] t$, as calibrated from preliminary measurements; and multiplied by the inverse of the relevant 2-by-2 response sub-matrix $\hat{\beta}$, as calibrated from measurements taken between experiments. Specifically, we took

$$\mathbf{F}(t) = \hat{\beta}^{-1}\left[\mathbf{V}(t) - \mathbf{V}(t_0) - \mathbb{E}\left[\hat{\alpha}\right](t - t_0)\right], \tag{13}$$

with $t_0 = 0.8\,\mathrm{s}$, at which time the zero offset had stabilised and there was no external force on the instrumented plate, and with estimates for $\mathbb{E}\left[\hat{\alpha}\right]$ and $\hat{\beta}$ from calibration.

S6.2. Calibration

To estimate the mean drift vector $\mathbb{E}\left[\hat{\alpha}\right]$, we took 10 zero-load recordings, for each of which the force sensor's output was recorded over 110 s with no external force on the instrumented plate. Dividing by 100 the change in V_j over the 100 s after t_0, we calculated the $\hat{\alpha}$ for each recording, and recovered

$$\mathbb{E}\left[\hat{\alpha}_x\right] = (121 \pm 7)\,\mu\mathrm{V\,s^{-1}} \text{ and } \mathbb{E}\left[\hat{\alpha}_z\right] = (225 \pm 18)\,\mu\mathrm{V\,s^{-1}}, \tag{14}$$

with each error being the standard error in the sample mean, as described in S9.

To estimate the response matrix $\hat{\beta}$, we took four static-load recordings before each set of experiments at a given channel incline $\tan\theta$ and release gate height h_g, and four after. For each recording, we attached a cradle to the centre of the instrumented plate with double-sided tape, then recorded the force sensor's output over 5 s, adding to the cradle, 1 s to 2 s after starting, 10 metal plates with combined mass $M_c = 442.3\,\mathrm{g}$. Calculating, for each recording, over all t between 3 s and 4 s, the average voltage response $\mathbf{V}^r = \langle \mathbf{V}(t) - \mathbf{V}(t_0) - \mathbb{E}[\hat{\alpha}]\,(t - t_0)\rangle_{\Delta t}$, we calculated over all such $\mathbf{V}^r$ the least-squares best-fit matrix $\hat{\beta}$ for the linear model $\mathbf{V}^r = \hat{\beta} M_c g(\sin\theta, \cos\theta)$, with gravity $g = 9.81\,\mathrm{m\,s^{-2}}$. The result was

$$\begin{pmatrix} \hat{\beta}_{xx} & \hat{\beta}_{xz} \\ \hat{\beta}_{zx} & \hat{\beta}_{zz} \end{pmatrix} = \begin{pmatrix} 0.83102 & -0.03522 \\ -0.13462 & 0.35345 \end{pmatrix} \mathrm{V\,N^{-1}}, \tag{15}$$

with the fit achieved by the linear model plotted in Figure S3.

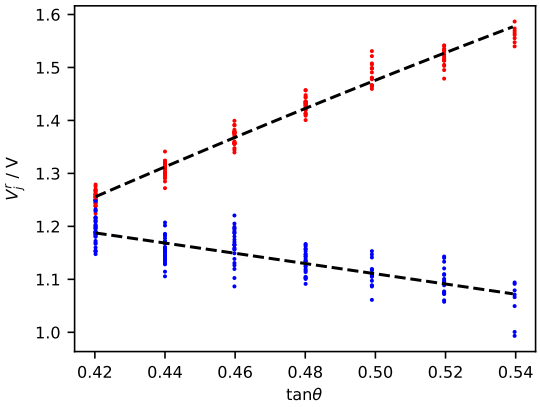

Figure S3. *The force sensor's response to static loads.* Points represent the voltage response of the downslope (red) and plate-normal (blue) outputs of the force sensor's charge amplifier, to an $M_c g = 4.34\,\mathrm{N}$ vertical load on the plate's centre, at different channel inclines $\tan\theta$. Lines represent the theoretical response, for a best-fit response matrix $\hat{\beta}$. Scatter arises from variations in $\hat{\alpha}$ from its expected value and from imperfections in the centering of the load.

S6.3. Validation

Since the measured effective friction on the plate μ is the ratio of time averages of the two inferred force components, it is particularly sensitive to this calibration, so we performed tests to validate the use of equation (13) and of the above values of $\mathbb{E}[\hat{\alpha}]$ and $\hat{\beta}$.

To test the measurement of the static friction between a volume of glass beads and the instrumented plate, we closed off the channel at its end and filled it with beads, recording the force sensor's voltage response to the resulting static load and calculating μ. To reduce the effect of $\hat{\alpha}$'s variability around its expected value, we repeated this measurement of μ three times and took the average, at each of a range of channel inclines θ between 15° and 25°. The resulting averages agreed with the theoretical values $\tan\theta$ to within both two mean standard errors and 10 %.

To test the measurement of dynamic friction, we released weighted sledges from rest at the top of the instrumented plate, inferring their accelerations from high-speed-camera footage and comparing the implied friction coefficients between the sledges and the plate to those measured with the force sensor. If $\hat{\mu}$ is the true, constant friction coefficient between a sledge and the plate, it will be linked to the time T for the front of the sledge to cross the instrumented plate by $X = g(\sin\theta - \hat{\mu}\cos\theta)T^2/2$, so we manually extracted T from the camera footage, calculated the implied value of $\hat{\mu}$, and compared it to the effective friction measured over the 4 s after t_0. We repeated the test three times for each of three sledges, with bases of printer paper, plastic mesh, and wetted tissue paper, and corresponding implied friction coefficients $\hat{\mu} = 0.227{\pm}0.002$, $0.340{\pm}0.008$, and $0.468{\pm}0.010$, released at channel inclines $\tan\theta = 0.3648$, 0.5609, and 0.6852, respectively, and in each case the average value of μ agreed with $\hat{\mu}$ to within two mean standard errors and 15 %, despite significant variation of the instantaneous value of F_x/F_z.

S7. Calculation of the Power Spectrum of the Basal Force Applied by the Flow

Here, we describe our derivation, calibration, and validation of a relation between a) the power spectrum of the basal force applied by the flow to the instrumented plate, and b) the measurements of the accelerometers on the bottom of the plate.

S7.1. Derivation

To derive such a relation, we consider the deformation of the instrumented plate in response to a single impact's force; calculate the contribution of that response to the mean seismic energy within the plate; consider the total mean seismic energy, due to multiple impacts; and link that energy to the measurements of accelerometers.

Since the steel structure of the plate is thin, stiff, and elastic, we may assume that linear Kirchhoff-Love plate theory applies in calculation of its deformation (Love & Darwin, 1888; Ciarlet, 1997). We further assume isotropy and homogeneity of the steel. Writing ρ_p, E_p, ν_p, X, Y, and H for the steel's density, Young's modulus, Poisson's ratio, length, width, and thickness, and defining its bending stiffness $D = E_p H^3/12(1-\nu_p^2)$, then its normal displacement w satisfies

$$D\nabla^2\nabla^2 w = -\rho_p H \partial_t^2 w + p, \tag{16}$$

for p the normal force per unit area to which the plate is subject. The relevant boundary conditions in our case are a clamped centre and free edges forming a rectangle. Now, on the set of functions satisfying these conditions, the left-hand-side operator in equation (16) is self-adjoint, so that we may define an orthonormal basis of eigenfunctions $\psi_j(\mathbf{x})$ with corresponding positive, real eigenvalues $4\pi^2\rho_p H f_j^2$, and may write $w_j(t)$ for the components of w with respect to this basis. Substituting into equation (16), the orthonormality of the basis functions allows us to recover the ordinary differential equation

$$\left(\frac{d^2}{dt^2} + 4\pi^2 f_j^2\right) w_j = \frac{1}{\rho_p h X Y}\int_{XY} \psi_j p \;\mathrm{d}^2\mathbf{x}. \tag{17}$$

If we impose $w = 0$ for $t < -T$, and suppose p represents an impact, so is a point force at $\mathbf{x}_0$ with support $[-T, 0]$, then we can solve this equation using the Green's function for the left-hand differential operator, $G(t;\tau) = \sin(2\pi f_j[t-\tau])/2\pi f_j$. Writing $p(\mathbf{x},t) = \delta(\mathbf{x}-\mathbf{x}_0)F_i(t)$ for Dirac delta function δ and plate-normal impact force F_i, and writing the sine function as a sum of exponentials, we recover that for $t > 0$

$$\begin{aligned} w_j(t) &= \int_{-\infty}^{t} \frac{\psi_j(\mathbf{x_0})}{4\pi i \rho_p H X Y f_j}\left(e^{2\pi i f_j(t-\tau)} - e^{-2\pi i f_j(t-\tau)}\right) F_i(\tau)\;\mathrm{d}\tau \\ &= \frac{\psi_j(\mathbf{x_0})}{2\pi\rho_p H X Y f_j}\Im\left[e^{2\pi i f_j t}\tilde{F}_i(f_j)\right], \end{aligned} \tag{18}$$

where $\tilde{\cdot}$ denotes a Fourier transform and $\Im[\cdot]$ the imaginary component, and we assume that F_i is real, so that $\tilde{F}_i(-f) = \tilde{F}_i(f)^*$.

We calculate the expected contribution of this response to the plate's mean seismic energy by assuming that the impacts are equally likely anywhere on the plate, and that energy is linearly attenuated, with quality factor $Q \gg 1$. We note that each eigenfunction component $w_j\psi_j$ behaves like a simple harmonic oscillator and that the eigenfunctions' orthogonality allows the energy of each component to be considered separately. Therefore, writing $\langle\cdot\rangle_{1/f_j}$ for time averages over the modes' cycles, the expected mean seismic energy in the plate, per unit area, due to the impact and immediately after it, will be

$$\begin{aligned}\mathcal{E}_i(0) &= \frac{1}{X^2Y^2}\int_{XY}\mathrm{d}\mathbf{x}_0\int_{XY}\mathrm{d}\mathbf{x}\sum_j \rho_p H\langle\dot{w}_j^2\psi_j^2\rangle_{1/f_j}\\ &= \sum_j \frac{|\tilde{F}_i(f_j)|^2}{2\rho_p H X^2Y^2},\end{aligned} \tag{19}$$

where again we have used the orthonormality of the basis functions. Linear attenuation will result in the exponential decay of this energy over time, with the jth mode's contribution having decay constant $2\pi f_j/Q$. For any time interval Δt starting before $t = 0$ and lasting until $t \gg Q/2\pi\min(f_j)$, the mean seismic energy in the plate over this time interval will therefore be

$$\langle\mathcal{E}_i\rangle_{\Delta t} \approx \sum_j \frac{Q|\tilde{F}_i(f_j)|^2}{4\pi\rho_p H X^2Y^2 f_j\Delta t}. \tag{20}$$

We note that only for $f_jT > Q/2\pi$ will a) attenuation affect the response during the interval $[-T, 0]$, and b) this interval be significant in the averaging, and we ignore such high frequencies, at which $|\tilde{F}_i(f_j)|^2$ will be negligible: for a Hertzian impact with $Q = 100$, $f_jT > Q/2\pi$ implies that $|\tilde{F}_i(f_j)|^2/|\tilde{F}_i(0)|^2 < 10^{-9}$.

To consider the plate's total energy rather than the contributions of individual impacts, we also restrict our attention to frequencies at which both individual impacts' forces and the responses to those forces are uncorrelated, as discussed in S2. Consequently, we can relate the total normal force on the plate F and the plate's total energy per unit area $\mathcal{E}$, over time Δt, to the contributions F_i and $\mathcal{E}_i$ of individual impacts within Δt:

$$|\tilde{F}(f)|^2 = \sum_i |\tilde{F}_i(f)|^2, \qquad \langle\mathcal{E}\rangle_{\Delta t} = \sum_i \langle\mathcal{E}_i\rangle_{\Delta t}, \tag{21}$$

with cross terms making no net contribution and Fourier transforms taken over Δt. We can therefore sum equation (20) over all impacts to recover an expression for the plate's total energy in terms of the power spectrum $|\tilde{F}(f)|^2$ of the total force applied on the plate.

To link this power spectrum $|\tilde{F}(f)|^2$ to the measured vertical acceleration of the plate's steel structure, we assume that a) a proportion $\mathcal{P}$ of the plate's energy is associated with the steel's vertical deformation and b) $|\tilde{F}(f)|$ varies sufficiently slowly that we can estimate its values away from the plate's resonant frequencies f_j. The relevant frequency scale is the mean bandgap between eigenvalues of equation (16) in the case of simply supported boundaries, for which the eigenfunctions $\hat{\psi}_{jk}$ and eigenvalues $\hat{f}_{jk}$ are

$$\hat{\psi}_{jk}(x, y) = 4\sin\left(\frac{j\pi x}{X}\right)\sin\left(\frac{k\pi y}{Y}\right), \tag{22}$$

$$\hat{f}_{jk} = \frac{\pi}{2}\left(\frac{j^2}{X^2} + \frac{k^2}{Y^2}\right)\sqrt{\frac{D}{\rho_p H}}. \tag{23}$$

Noting that the number of eigenvalues less than $\pi R^2\sqrt{D}/2\sqrt{\rho_p H}$ may be approximated by the area of a quarter-ellipse with major and minor axes XR and YR, this mean bandgap is

$$\Delta_f = \frac{2}{XY}\sqrt{\frac{D}{\rho_p H}}, \tag{24}$$

which will be equal to the corresponding asymptotic mean bandgap of the eigenvalues f_j for our problem, on the same domain. We use this to approximate the discrete spectrum on the right-hand side of equation (20) with a continuous spectrum; we approximate the left-hand side's mean seismic energy $\langle\mathcal{E}\rangle_{\Delta t}$ using a moving average $\langle|\tilde{a}(f)|^2\rangle_{\Delta f}$, over a frequency scale $\Delta f \gg \Delta_f$, of the mean spectral density of the steel's vertical acceleration. Recalling that the vertical acceleration accounts for only a proportion $\mathcal{P}$ of the total energy, we recover

$$\frac{1}{\mathcal{P}\Delta t}\int_{-\infty}^{\infty}\rho_p H\frac{\langle|\tilde{a}(f)|^2\rangle_{\Delta f}}{(2\pi f)^2}\,\mathrm{d}f \approx \int_0^{\infty}\frac{Q|\tilde{F}(f)|^2}{4\pi\rho_p H X^2Y^2 f\Delta_f\Delta t}\,\mathrm{d}f, \tag{25}$$

for both Fourier transforms restricted to the interval Δt. Consequently, noting that $a(t)$ is real and so $|\tilde{a}(f)|^2$ is symmetric, and approximating its value with the measurements a_k of the four accelerometers, our estimate of the power spectrum of the basal force applied by the flow to the instrumented plate is

$$P_F(f) = \frac{|\tilde{F}(f)|^2}{\Delta t} \approx \frac{(\rho_p H)^{3/2}XY\sqrt{D}}{\pi\mathcal{P}Qf\Delta t}\langle\sum_{k=1}^{4}|\tilde{a}_k(f)|^2\rangle_{\Delta f}. \tag{26}$$

With the accelerometers' calibrated sensitivities s_k taken from their calibration sheets, and the accelerometers' conditioning amplifier having amplification A, as defined in S4, the power spectral densities $|\tilde{a}_k|^2$ of the measured accelerations were calculated from the amplifier's output voltages V_k as

$$|\tilde{a}_k(f)|^2 = \frac{\Gamma(f)}{(As_k)^2}|\tilde{V}_k(f)|^2, \tag{27}$$

where $\Gamma(f) = 1 + (f/f_M)^n$ is a high-frequency correction for the accelerometers' non-contant frequency response and for the amplifier band-pass filter mentioned in S4, with f_M and n determined by the calibration described in section S7.3.

S7.2. Calibration

To calibrate the values of $\mathcal{P}$ and Q, and to extend the frequency range in which $|\tilde{a}_k|^2$ could be measured correctly, by calibrating f_M and n in Γ, we used the impacts of individual 2-mm-diameter glass beads, dropped onto random positions on the instrumented plate from a height of $h_i = 1\,\mathrm{m}$, with the channel inclined at $\theta = 0°$. The use of ball impacts to calibrate sensors is suggested in e.g. McLaskey and Glaser (2010), and allows calibration over frequency and force scales directly relevant to our experiments.

To record and analyse data, we used automatic triggers to record the voltage outputs of the accelerometers' conditioning amplifier throughout and after each of 25 impacts, at 250 kHz over 0.06 s, with amplification $A = 1.67\,\mathrm{V\,pC^{-1}}$. We divided these voltages by A and by the accelerometers' documented sensitivities $s_1 = 6.75\,\mathrm{fC}/(\mathrm{m\,s^{-2}})$, $s_2 = 5.61\,\mathrm{fC}/(\mathrm{m\,s^{-2}})$, $s_3 = 5.38\,\mathrm{fC}/(\mathrm{m\,s^{-2}})$, and $s_4 = 6.58\,\mathrm{fC}/(\mathrm{m\,s^{-2}})$, to recover the band-pass-filtered acceleration measurements $\hat{a}_k(t)$. To consider individual frequency components of these accelerations at maximum precision in both the frequency and time domains, we calculated their wavelet transforms using unit Gabor wavelets with centre

frequencies f_0 between 256 Hz and 125 kHz and standard deviations in frequency space $\sigma_{f_0} = f_0/4\pi$:

$$\mathcal{W}[\hat{a}_k](f_0, t_0) = \left(\frac{f_0^2}{2\pi}\right)^{1/4} \int_{-\infty}^{\infty} \hat{a}_k(t) e^{-\frac{f_0^2(t-t_0)^2}{4}} e^{2\pi i f_0 (t-t_0)} \, \mathrm{d}t. \tag{28}$$

We then calculated the corresponding spectral density, locally averaged around each f_0, of the plate's steel structure's vertical-displacement-associated seismic energy per unit area:

$$\hat{\Psi}_{f_0}(t) = \frac{1}{4} \sum_{k=1}^{4} \frac{\rho_p H |\mathcal{W}[\hat{a}_k](f_0, t)|^2}{(2\pi f_0)^2}, \tag{29}$$

for $\rho_p = 7800\,\mathrm{kg\,m^{-3}}$ and $H = 2\,\mathrm{mm}$. To extract the energy spectral density $\hat{\Psi}^0_{f_0}$ immediately after each impact, and the decay rate k_{f_0} of the spectral density over time, we performed a linear regression of $\ln \hat{\Psi}_{f_0}$ against t, over the time following the impact for which the signal was above the level of noise. An example for a single impact and wavelet is shown in Figure S4a, while Figure S4b shows the resulting average decay rates $\langle k_{f_0} \rangle$, over all 25 impacts, and Figure S4c shows the similarly averaged post-impact energy spectral densities $\langle \hat{\Psi}^0_{f_0} \rangle$.

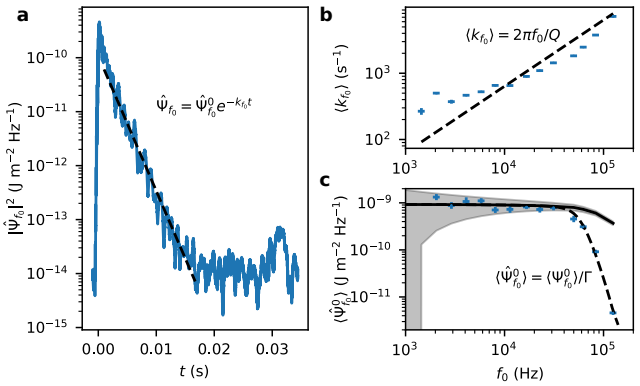

Figure S4. *The accelerometers' response to individual impacts of glass beads.* a) The plate's steel structure's vertical-displacement-associated seismic energy density $\hat{\Psi}_{f_0}$, localised around $f_0 = 8.1\,\mathrm{kHz}$, as inferred from uncalibrated accelerometer measurements for a single impact, decays exponentially. The dashed line indicates the linear regression of $\ln \hat{\Psi}_{f_0}$ against t, allowing extraction of the post-impact energy spectral density $\hat{\Psi}^0_{f_0}$, and the decay rate k_{f_0}. b) Points represent the mean decay rates $\langle k_{f_0} \rangle$ over 25 impacts. The dashed line indicates the theoretical relation, for best-fit quality factor Q. c) Points represent the mean measured post-impact energy spectral densities $\langle \hat{\Psi}^0_{f_0} \rangle$, over 25 impacts. The solid line indicates the theoretical value $\langle \Psi^0_{f_0} \rangle$ for a flat accelerometer response and for fitted $\mathcal{P} = 0.25$; the solid area its theoretical standard error; and the dashed line the theoretical relation for the best-fit high-frequency response correction $\Gamma(f) = 1 + (f/f_M)^n$. In both b and c, vertical and horizontal errorbars indicate the mean standard error over different impacts and the wavelet standard deviation in frequency space, respectively.

We used these data to perform the calibration, recovering the quality factor $Q = 99 \pm 12$ as the mean of $2\pi f_0 / \langle k_{f_0} \rangle$, and calibrating $\mathcal{P}$, f_M and n by comparing the measured values $\langle \hat{\Psi}^0_{f_0} \rangle$ to the theoretical values of the plate's total post-impact energy spectral density $\langle \Psi^0_{f_0} \rangle / \mathcal{P}$ predicted by equation (19) and the Hertz theory described in S3. Specifically, we noted that each dropped glass bead impacted, vertically, a glass bead attached to the plate in an approximately hexagonal packing, and we calculated the resulting random distribution of the angle θ_i between the vertical and the normal between impacted and impacting beads. To simulate an impact, we pulled θ_i from this distribution and took the spectral density of the applied plate-normal force to be

$$|\tilde{F}(f)|^2 = |\tilde{F}_n(f; \cos\theta_i \sqrt{2gh_i})|^2 \cos^2\theta_i, \tag{30}$$

for $F_n(t; u_n)$ the Hertzian normal force between two spheres colliding at normal velocity u_n and with the glass beads' material properties: density $\rho = 2500\,\mathrm{kg\,m^{-3}}$, diameter $d = 2\,\mathrm{mm}$, Young's modulus $E = 63\,\mathrm{GPa}$, and Poisson's ratio $\nu = 0.23$. By S3, this spectral density varies over frequency scales $\hat{f}_c/\tau \approx 100\,\mathrm{kHz} \gg \sigma_{f_0}$, so equation (19) implies that the impact imparts energy with expected spectral density around f_0

$$\frac{\Psi^0_{f_0}}{\mathcal{P}} \approx \frac{|\tilde{F}(f_0)|^2}{4\rho_p H X^2 Y^2 \Delta_f}, \tag{31}$$

for mean bandgap Δ_f given by equation (24) using the steel structure's material properties: density $\rho_p = 7800\,\mathrm{kg\,m^{-3}}$, length $X = 0.18\,\mathrm{m}$, width $Y = 0.1\,\mathrm{m}$, thickness $H = 2\,\mathrm{mm}$, and bending stiffess $D = E_p H^3/12(1-\nu_p^2)$ for Young's modulus $E_p = 200\,\mathrm{GPa}$ and Poisson's ratio $\nu_p = 0.29$. We calculated $\langle \Psi^0_{f_0} \rangle / \mathcal{P}$ as the average of $\Psi^0_{f_0}/\mathcal{P}$ over 25 simulated impacts, and noted that the dominant source of systematic error in its value was the varying number of resonant frequencies in each wavelet's frequency range, approximated as the 95 % confidence interval $f_0 \pm 2\sigma_{f_0}$. We therefore estimated the error by supposing this number had a Poisson distribution with mean $4\sigma_{f_0}/\Delta_f$. Finally, we calculated $\mathcal{P} = 0.25$ for consistency between measured $\langle \hat{\Psi}^0_{f_0} \rangle$ and theoretical $\langle \Psi^0_{f_0} \rangle$ at low f_0, and the least-squares best-fit values $f_M = 60\,\mathrm{kHz}$ and $n = 6$ for the correction to the high-frequency response of the accelerometers and accelerometer amplifier:

$$\langle \Psi^0_{f_0} \rangle / \langle \hat{\Psi}^0_{f_0} \rangle = \Gamma(f_0) = 1 + (f_0/f_M)^\alpha. \tag{32}$$

S7.3. Validation

We performed a different set of impact experiments to verify 1) the acoustic isolation of the instrumented plate from the rest of the channel - that only impacts on the plate made significant contributions to its normal displacement - and 2) the validity of equation (26) for the vertical basal force's spectral density $|\tilde{F}|^2$, with equation (27) for the measured accelerations and with $\mathcal{P} = 0.25$, $Q = 99$, $f_M = 60\,\mathrm{kHz}$, and $n = 6$. With the channel flat, we dropped steel ball bearings of diameter $(3.125 \pm 0.007)\,\mathrm{mm}$ from a metal plate $(100.68 \pm 0.02)\,\mathrm{mm}$ above the channel bed, onto a) 10 random positions on the plate, and b) 10 random positions off the plate, 10 mm from its edge. Having used automatic triggers to record the voltage output of the accelerometers' conditioning amplifier throughout and after the impact, at 250 kHz over 0.04 s, with amplification $A = 0.527\,\mathrm{V\,pC^{-1}}$ in case a and $16.7\,\mathrm{V\,pC^{-1}}$ in case b, we calculated in each case the inferred spectral density $|\tilde{F}|^2$ of the basal force. This is plotted, and in case a compared to its theoretical value, in Figure S5.

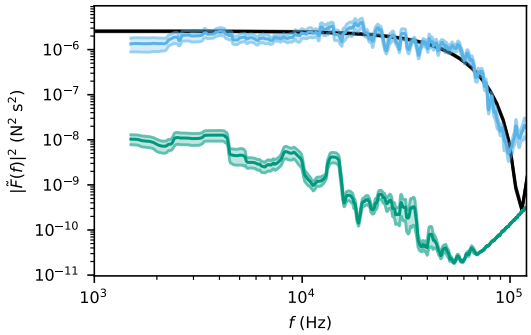

Figure S5. *The inferred spectrum of the vertical basal force applied by a ball bearing's impact.* Using appropriate material parameters and calibrated $\mathcal{P}$, Q, f_M and n, the spectral density calculated using equations (26) and (27) for an on-plate impact (blue) is consistent with the theoretical spectral density (black) at all frequencies at which the accelerometers' signal is distinguishable from noise. Under the same conditions, the contributions from an off-plate impact (green) are less than 1 % of those from an on-plate impact. All error regions represent the mean standard errors over different impacts.

Figure S5 shows that 1) the plate is acoustically isolated from the rest of the channel, and 2) equations (26) and (27) are valid for $\mathcal{P} = 0.25$, $Q = 99$, $f_M = 60\,\mathrm{kHz}$, and $n = 6$. The contributions of off-plate impacts to $|\tilde{F}|^2$ are less than 1 % of the contributions of on-plate impacts, and the values of $|\tilde{F}|^2$ inferred using sections S7.1 and S7.2 are consistent with the theoretical values $|\tilde{F}_H|^2$, calculated using the Hertz theory that is described in S3, for the impact of a spherical steel ball bearing ($\rho_1 = 7800\,\mathrm{kg\,m^{-3}}$, $d_1 = 3.125\,\mathrm{mm}$, $E_1 = 200\,\mathrm{GPa}$, $\nu_1 = 0.29$) on a spherical glass bead ($\rho_2 = 2500\,\mathrm{kg\,m^{-3}}$, $d_2 = 2\,\mathrm{mm}$, $E_2 = 63\,\mathrm{GPa}$, $\nu_2 = 0.23$), with impact normal an angle θ_i from the vertical (taken from a random distribution for uniformly distributed impacts of a d_1-diameter particle on a hexagonal packing of d_2-diameter particles) and normal velocity $\cos\theta_i\sqrt{2gh_i}$ (for gravitational acceleration $g = 9.81\,\mathrm{m\,s^{-2}}$ and drop height $h_i = 0.1\,\mathrm{m}$). Discrepancies between theory and observations indicate systematic relative error, due to errors in our attenuation model and variability in the density of the plate's resonant frequencies, which can be estimated as $|\tilde{F}|^2/|\tilde{F}_H|^2 - 1$.

S8. Sidewall Image Processing

To extract profiles of the flow's kinematic properties at the channel wall, we performed five stages of image processing: calibration, particle detection, particle tracking, velocity smoothing, and coarse graining.

Firstly, at each channel incline $\tan\theta$, following camera alignment, we calibrated distances on camera images by capturing an image of a calibration sheet, attached to the inside of the channel wall and covered with a 10 mm chequered pattern. We convolved the greyscale image matrix with an ideal corner pattern; identified corner locations as the weighted centroids of above-threshhold regions of the convolution product; and calculated the mean number of pixels between corners horizontally and vertically to determine the correspondance between distances on the channel wall and in its images. The inferred resolution was approximately $8\,\mathrm{px\,mm^{-1}}$.

Secondly, within each image captured during steady flow, we identified the locations of particles by convolving the greyscale image matrix with a 'typical' particle pattern from a calibration image. The pattern was selected by hand-labelling 25 particles in one image at each channel inclination, and taking the average of their 18×18 greyscale image matrices. Each peak of the Gaussian-smoothed convolution product was taken to correspond to a particle, located at the local peak of the unsmoothed convolution product. We achieved sub-pixel resolution by fitting Gaussian curves to the local horizontal and vertical variation of the convolution product, about the pixel-resolution peak. This method identified the correct locations of around 90 % of particles visible at the channel wall, robust to specular reflections and variations in lighting.

Thirdly, we tracked particles from one frame to the next by associating each particle identified in each image with the closest particle identified in the previous image, under the conditions that a) the association was not many-to-one, with closer particles having priority, and b) the implied velocity was lower than a $1.2\,\mathrm{m\,s^{-1}}$ limit. This velocity limit corresponded to displacement per frame of one third of a particle diameter, and was more than two standard deviations above the root mean square particle velocity even for the fastest flows.

Fourthly, for each tracked particle, we adjusted for the effect of varying specular reflections on its location estimates, by smoothing the particle velocity over a moving, five-frame window, using a robust weighted least-squares local linear regression. The use of sub-pixel location estimation permitted the use of the robust method, assigning lower weight to outliers, while the linear regression corresponded to finding the best-fit constant acceleration within each 2.5 ms window.

Finally, we used coarse-graining to infer continuum profiles from the point distributions of particle velocities. From the particles' base-normal positions z_j and smoothed velocities $\mathbf{u}_j$, we estimated the downslope-averaged and time-averaged base-normal profiles, at the channel's wall, of relative volume fraction $\phi_w(z)$, mean velocity $\mathbf{u}_w(z)$, and granular temperature $T_w(z)$ as

$$\phi_w(z) = \langle \sum_j C(z_j; z)\pi d^2/4 \rangle_{\Delta t_c} \tag{33}$$

$$\mathbf{u}_w(z) = \langle \sum_j C(z_j; z)\pi d^2 \mathbf{u}_j/4 \rangle_{\Delta t_c}/\phi_w(z) \tag{34}$$

$$T_w(z) = \langle \sum_j C(z_j; z)\pi d^2 ||\mathbf{u}_j - \mathbf{u}(z)||^2/4 \rangle_{\Delta t_c}/\phi_w(z) \tag{35}$$

for averages $\langle\cdot\rangle_{\Delta t_c}$ over all frames recorded by the camera, sums $\sum_j \cdot$ over all particles detected in each frame, and weighting function C localised around z, with integral over the total spatial domain equal to 1. This process is discussed for general C in Babic (1997), but we took Gaussian profiles

$$C(z'; z) = \frac{1}{\Phi(z/\sigma_z)\Delta x\sqrt{2\pi\sigma_z^2}} \exp\left[-\frac{(z-z')^2}{2\sigma_z^2}\right], \tag{36}$$

for $\sigma_z = d/2$ the coarse-graining width, Δx the downslope extent over which images were captured, and Φ the cumulative distribution function of the standard normal distribution, accounting for the impossibility of detecting particles below the base's surface.

S9. Statistical Tools

S9.1. Standard Errors

In sections S6.2, S6.3, S7.2, and S7.3, the standard error in the sample mean (or mean standard error) over repeated measurements $(y_j)_{j=1}^n$, with mean $\bar{y}$, is defined by

$$\sigma_m = \frac{1}{\sqrt{n}}\left[\sqrt{\frac{1}{n-1}\sum_{j=1}^{n}(y_j - \bar{y})^2}\right]. \tag{37}$$

Considering measurements as independent and identically distributed random variables, $n\sigma_m^2$ is an unbiased estimator for the variance of the distribution from which they are taken, provided the latter is finite, and so σ_m^2 is an unbiased estimator for the variance of $\bar{y}$, considered as a random variable. Under this model, assuming certain regularity conditions, the central limit theorem implies that $\bar{y}$ is taken from an approximately normal distribution, with true expectation μ equal to the expectation of y_j. Consequently, σ_m is a typical error for the estimation of μ by $\bar{y}$, in the sense that it's the scale by which confidence intervals for μ can be derived from the percentage points of the standard normal distribution. For example, $\bar{y} \pm \sigma_m$ is an approximate 68 % confidence interval for μ, while $\bar{y} \pm 2\sigma_m$ is an approximate 95 % confidence interval.

S9.2. Fitting a Model's Free Parameters

In seeking the free parameter values for which a model's predictions $\hat{P}_F^0$ best fit our observations P_F^0, we are concerned with the ratio between predictions and observations, and wish to penalise underestimates by a given factor as much as overestimates by that factor. Rather than considering the arithmetic error $P_F^0 - \hat{P}_F^0$, which places excessive weight on predictions' agreement with large values P_F^0, or the fractional error $1 - \hat{P}_F^0/P_F^0$, which penalises overestimates more than underestimates, we therefore consider the logarithmic error $\ln(P_F^0/\hat{P}_F^0)$. To penalise large errors more than small errors, we take a quadratic loss function, and seek to minimise

$$\epsilon = \exp\left[\sqrt{\frac{1}{N}\sum \ln^2\left(P_F^0/\hat{P}_F^0\right)}\right], \tag{38}$$

the geometric standard error over the $N = 57$ predictions. This may be interpretted as a typical factor by which predictions are greater or lesser than observations.

To understand this parameter fitting within a statistical framework, and to make rigorous the sense in which ϵ is 'typical', we note that our measurements are subject to a large number of approximately independent multiplicative errors, so that observations P_F^0 may be expected to be approximately log-normally distributed about the predictions $\hat{P}_F^0(\theta_0)$ of an accurate model with accurate free parameter value θ_0. Under this statistical model, the likelihood may be written as a function of the free parameter θ and the log-normal distribution's shape parameter σ as

$$\mathcal{L}\left(\theta, \sigma | \ln P_F^0\right) = \prod \frac{1}{\sqrt{2\pi\sigma^2}} \exp\left[-\frac{\ln^2(P_F^0/\hat{P}_F^0(\theta))}{2\sigma^2}\right]. \tag{39}$$

By considering $\ln \mathcal{L}$, we can see that choosing the parameter value that minimises $\ln \epsilon$, and so ϵ, is equivalent to using the maximum likelihood estimator for θ. Similarly, the maximum likelihood estimator for σ^2 is $\ln^2 \epsilon$, equal to the mean square value of $\ln(P_F^0/\hat{P}_F^0)$. Under this model, with these parameters, ϵ will be the typical geometric error in the same sense that σ_m is typical in section S9.1: considering the percentage points of the normal distribution, 68 % of observations P_F^0 will be within $\epsilon^{\pm 1}\hat{P}_F^0$, while 95 % will be within $\epsilon^{\pm 2}\hat{P}_F^0$.

S9.3. The Akaike Information Criterion

To compare physical models with differing numbers of free parameters, we use the Akaike information criterion. For each model predicting $\hat{P}_F^0$, we consider the statistical model discussed in section S9.2, in which $\ln P_F^0$ is normally distributed about $\ln \hat{P}_F^0$ with constant variance σ^2. We note that if the physical model has a number k of free parameters, the associated statistical model has $k + 1$ free parameters, due to the additional free parameter σ^2. Considering the likelihood $\mathcal{L}$ for this model, as defined in equation (39), the value of the Akaike information criterion is therefore (Akaike, 1971)

$$AIC = 2\left(k + 1 - \ln(\max \mathcal{L})\right). \tag{40}$$

The Akaike information criterion balances each of the five models' goodness of fit against the number of parameters varied to achieve that fit, with $AIC/2$ a good estimator for the information lost in describing the true data-generating process by the model under consideration. Akaike (1974) makes this rigorous, for the Kullback-Liebler sense of information (Kullback & Leibler, 1951), but in brief the model minimising AIC is preferred in an information theoretic sense, with $RL = \exp\left[(\min AIC - AIC)/2\right]$ the relative likelihood of any other model (Akaike, 1978).

Of the existing models for a flow's seismic signal, as described in section 1.2 and implemented in section 3.3, the 'thin-flow' model of Farin et al. (2019) is strongly preferred by the Akaike information criteria. All models' AIC and RL values are listed in Table S1. Results are identical when using Hurvich and Tsai (1989)'s correction to the Akaike information criterion, which avoids bias for finite sample sizes, under certain regularity conditions.

S10. The Green's Function's Effect on Signals' Energy and Relative Amplitude

Here, we use our experimental seismic signals to show that a signal's Green's function affects certain seismic properties that previous authors have used to describe geophysical flows directly: the rate of seismic energy emission and the relative amplitudes of different landquake signals with the same source and receiver locations.

For our experiments, the Green's function appears via equation (12) of the main text, which relates the basal forces exerted by the flow to the accelerations they caused and indicates that, on a larger, denser, stiffer, or more lossy plate, the same force would result in smaller accelerations and hence a smaller seismic signal. Similarly, working from the derivation of this equation in S7, the total high-frequency seismic power transferred by the flow to the plate is given in terms of the basal force's power spectral density P_F by

$$\Pi_s \approx \frac{1}{4\sqrt{\rho_p H D}} \int_{1\,\mathrm{kHz}}^{\infty} P_F(f)\, \mathrm{d}f, \tag{41}$$

dependent on plate density ρ_p, thickness H, and bending moment D. The proportion of flow energy dissipated by seismic emission is therefore a function of basal properties rather than of flow properties alone.

Furthermore, the Green's functions for seismic signals will depend differently on frequency f, so that basal properties

Table S1. *Model comparison with the Akaike information criterion.* For each of the existing physical models described in section 1.2, we list the number k of free parameters in its implementation in section 3.3; the value AIC of the Akaike information criterion for its associated statistical model; and this model's relative likelihood RL.

Model	k	AIC	RL
Kean et al. (2015)	1	204	6×10^{-17}
Lai, Tsai, Lamb, Ulizio, and Beer (2018)	0	284	3×10^{-34}
Farin et al. (2019) 'thick-flow'	1	181	7×10^{-12}
Farin et al. (2019) 'thin-flow'	1	129	1
Bachelet et al.	1	199	8×10^{-16}

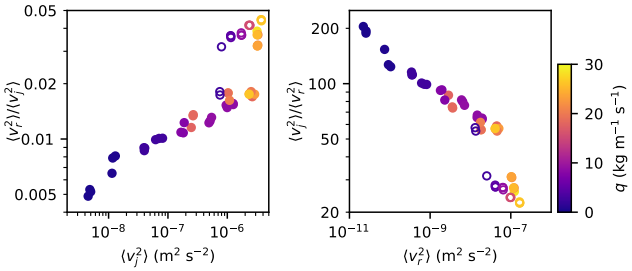

Figure S6. *Comparison between the mean squared seismic velocities $\langle v_j^2\rangle$ observed in our experiments and the mean squared velocities $\langle v_r^2\rangle$ that would be observed in an idealised geophysical context.* For the latter, we took $\rho_g = 2500\,\mathrm{kg\,m^{-3}}$, $c_s = 1\,\mathrm{km\,s^{-1}}$, and $r = 1\,\mathrm{m}$ in equation (42), but other values would change only the prefactor. Colours indicate each experiment's mass flux q per unit channel width, and unfilled symbols represent experiments for which the flow was in the transitional regime.

will affect even the relative signal amplitudes of different flows with the same Green's function. For illustration, we consider the vertical velocity response of a surficial receiver to a vertical, surficial point force, on an isotropic, homogeneous, perfectly elastic half-space with Poisson ratio 0.25, material density ρ_g and shear wave velocity c_s. For large source-receiver separation r, at leading order, Miller and Pursey (1954) showed the power spectral density P_{v_r} of this response to be related to the power spectral density P_F of the vertical basal force by

$$P_{v_r}(f) = \frac{1.20 f^3}{\rho_g^2 c_s^5 r} P_F(f), \tag{42}$$

which we compare to the mean velocity power spectral density over the accelerometers in our experiments,

$$\bar{P}_{v_j}(f) = \frac{1}{4\Delta t}\sum_{j=1}^{4}\left(\frac{|\tilde{a}_j(f)|}{2\pi f}\right)^2 \approx \frac{\mathcal{P}Q}{16\pi(\rho_p H)^{3/2} XY\sqrt{Df}} P_F(f). \tag{43}$$

The mean squared velocity at the receiver, being the integral of $P_{v_r}(f)$ over all f, will clearly be more sensitive to the corner frequency f_c of P_F than were the mean squared velocities observed in our experiments. Figure S6 shows the consequence: approximating mean squared velocities by integrating (42) and (43) between 1 kHz and f_c, there is no constant conversion factor between the mean square velocities observed in our experiments and those that would be observed if the same flows applied the same forces in an idealised geophysical context. Even among signals with the same source and receiver locations, the Green's function determines the ratios between different signals' amplitudes, so that a signal must be properly deconvolved to infer the properties of a flow's forces.

Movie S1.

Example of footage captured by the high-speed camera at the channel wall, as described in section 2.1. Footage was captured during the period of steady flow of an experiment at a channel incline $\tan\theta = 0.44$, with a release gate height $h_g = 5\,\mathrm{mm}$. The movie is a 0.5 s excerpt, vertically cropped and slowed by a factor of 20.

Movie S2.

Illustration of particle tracking velocimetry. Footage was captured during the period of steady flow of an experiment at a channel incline $\tan\theta = 0.48$, with a release gate height $h_g = 20\,\mathrm{mm}$. Superposed red dots indicate the particle centres located by the algorithm described in S8, while blue lines indicate particle trajectories reconstructed after that algorithm's particle tracking and velocity smoothing.

References

Akaike, H. (1971). *Determination of the number of factors by an extended maximum likelihood principle* (Tech. Rep.). Inst. Statist. Math.

Akaike, H. (1974). A new look at the statistical model identification. *IEEE Transactions on Automatic Control*, *19*(6), 716–723. Retrieved from `https://link.springer.com/content/pdf/10.1007%2F978-1-4612-1694-0.pdf`

Akaike, H. (1978). On the likelihood of a time series model. *Journal of the Royal Statistical Society. Series D (The Statistician)*, *27*(3/4), 217–235. Retrieved from `http://www.jstor.org/stable/2988185`

Arran, M. I., Mangeney, A., de Rosny, J., Farin, M., Toussaint, R., & Roche, O. (2021). *Laboratory landquakes, v1.0.* Zenodo. doi: 10.5281/zenodo.4044233

Babic, M. (1997). Average balance equations for granular materials. *International Journal of Engineering Science*, *35*(5), 523–548. Retrieved from `http://www.sciencedirect.com/science/article/pii/S0020722596000948` doi: 10.1016/S0020-7225(96)00094-8

Bertrand, J. (1878). Sur l'homogénéité dans les formules de physique. *Comptes rendus hebdomadaires des séances de l'Académie des sciences*, *86*(15), 916–920.

Buckingham, E. (1914). On physically similar systems; illustrations of the use of dimensional equations. *Physical Review*, *4*(4), 345–376.

Ciarlet, P. G. (1997). Chapter 1 - linearly elastic plates. In P. G. Ciarlet (Ed.), *Mathematical elasticity* (Vol. 27, p. 3–127). Elsevier. Retrieved from `http://www.sciencedirect.com/science/article/pii/S0168202497800070` doi: 10.1016/S0168-2024(97)80007-0

Farin, M., Tsai, V. C., Lamb, M. P., & Allstadt, K. E. (2019). A physical model of the high-frequency seismic signal generated by debris flows. *Earth Surface Processes and Landforms*, *44*(13), 2529–2543. Retrieved from `https://onlinelibrary.wiley.com/doi/abs/10.1002/esp.4677` doi: 10.1002/esp.4677

Hertz, H. R. (1881). Über die berührung fester elastischer körper. *Journal für die reine und angewandte Mathematik*, *92*, 156–171. Retrieved from `https://home.uni-leipzig.de/pwm/web/download/Hertz1881.pdf`

Hurvich, C. M., & Tsai, C.-L. (1989). Regression and time series model selection in small samples. *Biometrika*, *76*(2), 297–307. Retrieved from `https://doi.org/10.1093/biomet/76.2.297` doi: 10.1093/biomet/76.2.297

Kean, J. W., Coe, J. A., Coviello, V., Smith, J. B., McCoy, S. W., & Arattano, M. (2015). Estimating rates of debris flow entrainment from ground vibrations. *Geophysical Research Letters*, *42*(15), 6365–6372. Retrieved from https://agupubs.onlinelibrary.wiley.com/doi/abs/10.1002/2015GL064811 doi: 10.1002/2015GL064811

Kullback, S., & Leibler, R. A. (1951). On information and sufficiency. *Ann. Math. Statist.*, *22*(1), 79–86. Retrieved from https://doi.org/10.1214/aoms/1177729694 doi: 10.1214/aoms/1177729694

Lai, V. H., Tsai, V. C., Lamb, M. P., Ulizio, T. P., & Beer, A. R. (2018, 06). The seismic signature of debris flows: Flow mechanics and early warning at Montecito, California. *Geophysical Research Letters*, *45*(11), p5528–5535. doi: 10.1029/2018GL077683

Love, A. E. H., & Darwin, G. H. (1888). XVI. the small free vibrations and deformation of a thin elastic shell. *Philosophical Transactions of the Royal Society of London. (A.)*, *179*, 491–546. Retrieved from https://royalsocietypublishing.org/doi/abs/10.1098/rsta.1888.0016 doi: 10.1098/rsta.1888.0016

McLaskey, G. C., & Glaser, S. D. (2010). Hertzian impact: Experimental study of the force pulse and resulting stress waves. *The Journal of the Acoustical Society of America*, *128*(3), 1087–1096. Retrieved from https://asa.scitation.org/doi/abs/10.1121/1.3466847 doi: 10.1121/1.3466847

Michlmayr, G., & Or, D. (2014, October 01). Mechanisms for acoustic emissions generation during granular shearing. *Granular Matter*, *16*(5), 627–640. Retrieved from https://doi.org/10.1007/s10035-014-0516-2 doi: 10.1007/s10035-014-0516-2

Miller, G. F., & Pursey, H. (1954). The Field and Radiation Impedance of Mechanical Radiators on the Free Surface of a Semi-Infinite Isotropic Solid. *Proceedings of the Royal Society of London A: Mathematical, Physical and Engineering Sciences*, *223*(1155), 521–541. Retrieved from http://rspa.royalsocietypublishing.org/content/223/1155/521 doi: 10.1098/rspa.1954.0134